Supplementary Materials for

"Using Spontaneous Emission of a Qubit as a Resource for Feedback Control"

P. Campagne-Ibarcq,[1,2] S. Jezouin,[1,2] N. Cottet,[1,2] P. Six,[3,2] L. Bretheau,[1,2] F. Mallet,[1,2] A. Sarlette,[2] P. Rouchon,[3,2] and B. Huard[1,2]

[1]*Laboratoire Pierre Aigrain, Ecole normale supérieure, PSL Research University, CNRS, Université Pierre et Marie Curie, Sorbonne Universités, Université Paris Diderot, Sorbonne Paris-Cité, 24 rue Lhomond, 75231 Paris Cedex 05, France*

[2]*Quantic Team, INRIA Paris-Rocquencourt, Domaine de Voluceau, B.P. 105, 78153 Le Chesnay Cedex, France*

[3]*Centre Automatique et Systèmes, Mines ParisTech, PSL Research University, 60 Boulevard Saint-Michel, 75272 Paris Cedex 6, France.*

(Dated: July 27, 2016)

I. SYSTEM CHARACTERIZATION AND EXPERIMENTAL SETUP

A. Qubit dispersively coupled to a cavity mode

The qubit studied in this experiment follows the superconducting 3D transmon design [31] and was already used and described in Ref. [3] (note however that the qubit underwent several cycles to room temperature since then). It consists of a single aluminum Josephson junction connected to two 0.4×1 mm^2 antennas forming a large capacitance shunting the junction, so that it behaves as a weakly anharmonic resonator. The antennas couple to the electromagnetic field, so that the system can be driven with microwaves. By addressing only the transition between the ground and first excited states, we isolate an effective qubit at $f_q = 6.27$ GHz with anharmonicity $\alpha = 160$ MHz.
The transmon is embedded in a $26.5 \times 26.5 \times 9.5$ mm^3 copper cavity, anchored at the base-temperature (20 mK) of a dilution refrigerator. The system is probed via two transmission lines terminated with SMA connectors whose central pin dips inside the cavity. The cavity energy damping rate $\kappa/2\pi = 2.8$ MHz is dominated by the coupling to the "out" transmission line, $\kappa_{\text{out}} \simeq 0.9\ \kappa$, which is connected to the detector of qubit fluorescence. The first cavity mode (TE110, resonating at $f_c = 7.86$ GHz) dominates the electromagnetic environment of the transmon. Indeed, the transmon chip is placed at the maximum of the TE110 field and its antennas are aligned with the field polarization, whereas the next cavity mode (at 11.5 GHz) has an amplitude node at the transmon position. It has two important implications.

First, the qubit and cavity TE110 mode are strongly coupled and described by the dispersive hamiltonian [25]

$$H = hf_c a^\dagger a + hf_q \frac{\sigma_z}{2} - h\chi a^\dagger a \frac{\sigma_z}{2}, \tag{S1}$$

where the dispersive shift $\chi = 9.7$ MHz allows to modulate the qubit frequency ("FM box" in Fig. 1) according to the scheme described in Sec. I F based on AC-Stark effect [25, 26]. Second, by dressing the transmon states, the open cavity mode allows to implement a monitored dissipation channel. The qubit can indeed decay by emitting photons at f_q into the transmission lines probing the cavity [32] (see Fig. S1), by Purcell effect [17].

From continuous wave reflection and transmission measurements close to f_c, we find that thermal excitation of the qubit is negligible. Then the Lindblad master equation ruling the qubit density matrix ρ_0 dynamics reads

$$\frac{\mathrm{d}\rho_0(t)}{\mathrm{d}t} = -\frac{i}{\hbar}[H, \rho_0(t)] + \gamma_1 \mathcal{D}[\sigma_-]\rho_0(t) + \frac{\gamma_\phi}{2}\mathcal{D}[\sigma_z]\rho_0(t), \tag{S2}$$

where $\mathcal{D}$ is the Lindblad damping superoperator defined by $\mathcal{D}[L]\rho = L\rho L^\dagger - \frac{1}{2}L^\dagger L\rho - \frac{1}{2}\rho L^\dagger L$ and γ_ϕ is the dephasing rate. The latter reads $\gamma_\phi = \gamma^\star + \gamma_m = (22\ \mu\text{s})^{-1}$, where $\gamma^\star = (30\ \mu\text{s})^{-1}$ corresponds to pure dephasing and $\gamma_m = (84\ \mu\text{s})^{-1}$ corresponds to measurement induced dephasing by the *FM box* (see Sec. I F for more details).

B. Cryogenics

The low temperature and pure dephasing rate of the qubit are partly achieved through careful filtering and isolation of the transmission lines used to measure the system, Fig. S1.
On the one hand, the "Input" and "Reflection" lines, which allow to send microwaves to probe and drive the system,

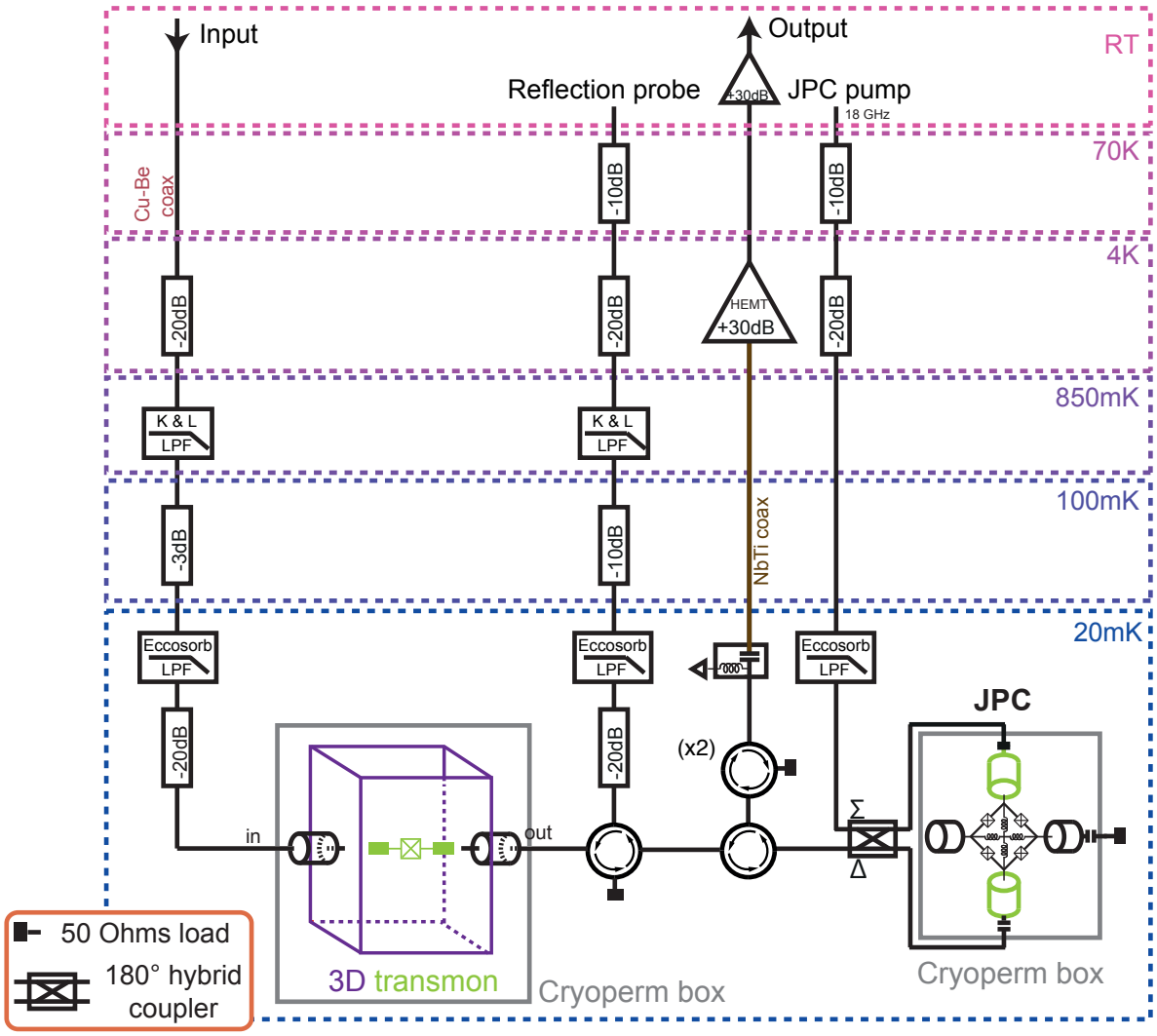

Figure S1: **Schematics of the refrigerator wiring.** Discrete attenuators (XMA corp.) are distributed along the microwave lines ("input", "reflection probe" and "JPC pump") in order to thermalize the signals at each stage. Filters are added to protect the 3D transmon from infrared radiation. The fluorescence field on the "out" line is amplified by reflection on the JPC and routed out of the fridge after further amplification. Circulators on the output lines isolate the system from the amplifier noise.

are heavily attenuated and filtered in order to ensure that negligible thermal excitations can reach the 3D transmon. A commercial low-pass filter (from K&L) with 12 GHz cut-off frequency is used at the still stage (850 mK), while a homemade low-pass filter consisting in a microstrip line enclosed in an infrared tight box filled with Eccosorb is inserted at base temperature.

On the other hand, several cryogenic circulators (Quinstar corp.) are placed at the output port of the 3D transmon in order to isolate it from the noise coming back from the amplifiers. The closest amplifier consists in a Josephson Parametric Converter [18, 19] (used as a near-quantum-limited non-degenerate preamplifier with +25 dB gain and 3.3 MHz bandwidth pumped at 14.8 GHz) followed by a low noise HEMT (High Electron Mobility Transistor) amplifier with 30 dB gain from Caltech University.

Protection from external magnetic noise is also achieved by enclosing the transmon copper 3D cavity and the JPC in a *cryoperm* shield and by further wrapping them in a superconducting aluminum foil to shield residual magnetic fields.

C. Measurement and feedback setup

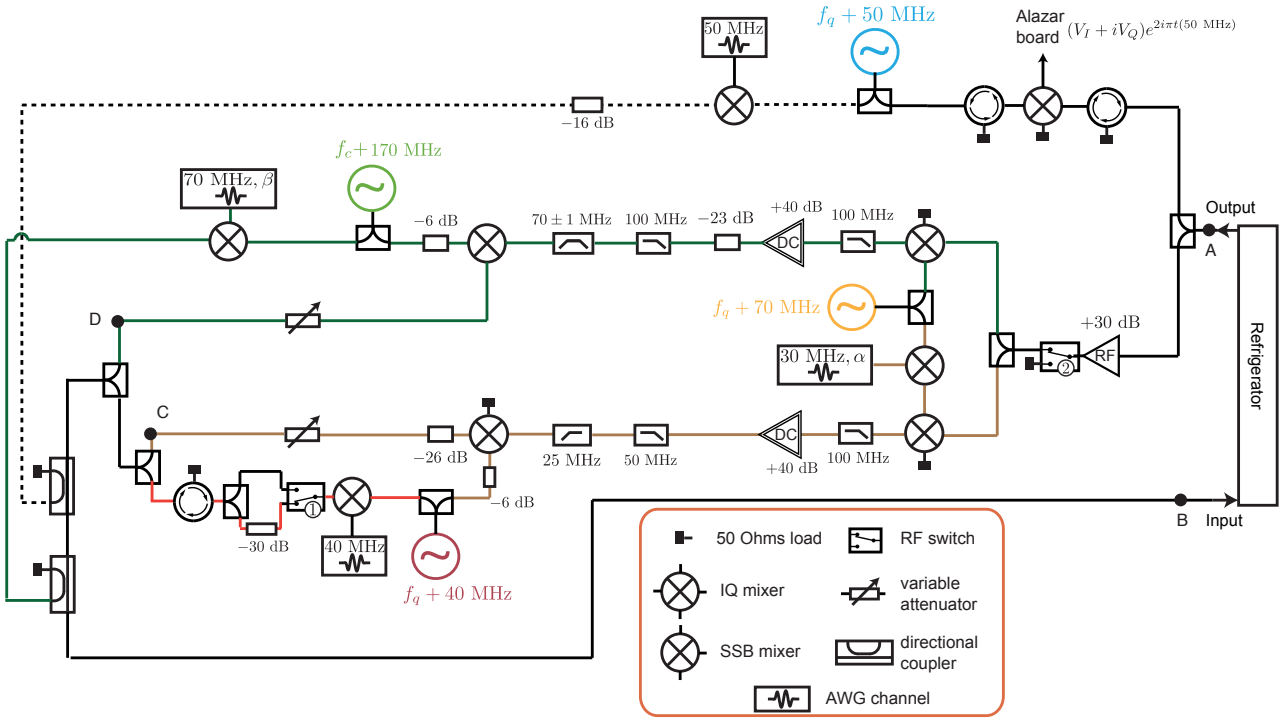

Figure S2: **Feedback and measurement setup schematics at room temperature**. The fluorescence signal that exits from the refrigerator is split to be used for qubit tomography at the end of each experiment and for implementing the three "boxes" of the feedback loop (see Fig. 1). We highlight in dark green (resp. brown, red) the part of the circuit corresponding to the *FM box* (resp. *Rabi box*, *drift box*). Frequency conversion of the signal is achieved by mixing the signals with properly attenuated LO's so that each mixer works with nominal input powers. Down-conversion allows for tighter band-pass filtering of the signals. Four different signal generators are used as LO's. Their relative phase drifts on the order of the hour, which needs to be corrected for, despite synchronization to a unique atomic clock reference.

The amplified signal at the output of the refrigerator is split in two parts (see Fig. S2). One part is used to perform tomographic measurement of the qubit state, while the other one is used as an input of the feedback loop.

- **Tomography of the qubit state** is performed through heterodyne detection of the fluorescence field amplitude once the feedback loop and driving of the qubit have been stopped, which is done using the RF-switch② and by turning off the 40 MHz signal of the AWG (bottom in Fig. S2, used to implement the *Drift box*). The fluorescence signal at f_q is first downconverted to 50 MHz by mixing it with a local oscillator (LO) at $f_q + 50$ MHz (in blue), then digitized at 500 MS.s^{-1} by an Alazar ATS9351 board and finally numerically demodulated and integrated over a time $T = 5$ μs. According to Eq. (1) and references [22, 34–36], the two obtained quadratures read, as a mean,

$$\begin{cases} \overline{V_{I,\mathrm{int}}} = \lambda \int_0^T \sqrt{\frac{\eta\gamma_1}{2}} \langle\sigma_x\rangle_t \mathrm{d}t = \lambda' \langle\sigma_x\rangle_0 \\ \overline{V_{Q,\mathrm{int}}} = \lambda \int_0^T \sqrt{\frac{\eta\gamma_1}{2}} \langle\sigma_y\rangle_t \mathrm{d}t = \lambda' \langle\sigma_y\rangle_0 \end{cases}, \tag{S3}$$

where λ is an *a priori* undetermined prefactor accounting for the overall gain of the detection setup and $\lambda' = \lambda\sqrt{\frac{\eta\gamma_1}{2}}\frac{1-e^{-\gamma_2 T}}{\gamma_2}$. The prefactor λ' is easily calibrated by preparing the qubit in $(|e\rangle + i|g\rangle)/\sqrt{2}$ corresponding to $\langle\sigma_y\rangle_0 = 1$. One can therefore access both $\langle\sigma_x\rangle$ and $\langle\sigma_y\rangle$. Measurement of $\langle\sigma_z\rangle$ is carried by first rotating the qubit state by $\pi/2$ around σ_y before measuring the quadratures V_I, V_Q, thus mapping $\langle\sigma_z\rangle$ to $\langle\sigma_x\rangle$. The rotation is achieved by applying a high power drive pulse at f_q which is generated by single side-band mixing of an LO at $f_q + 40$ MHz (in red) with a 40 MHz windowed waveform from an Arbitrary Waveform Generator (AWG) 5014B by Tektronix. In order to get high fidelity of the qubit rotation, the pulse was short and intense, thanks to an RF-switch① that allows to avoid the following 30 dB attenuator. Note that tomography through heterodyne measurement of the fluorescence was preferred to more usual dispersive measurement of the cavity

because in our case the nearly-quantum-limited JPC preamplifier is centered at f_q and not f_c. We however explicitly verified that dispersive measurements yield identical results as fluorescence measurements. To do so, the "blue" LO was set at $f_c + 50$ MHz, and was used both to generate and measure microwave pulses at f_c (dotted transmission line) transmitted across the cavity.

- **The feedback loop** starts by amplifying the signal coming from the refrigerator and splitting it in two parts. The lower one on Fig. S2 implements the *Rabi box* while the upper one implements the *FM box*. In the *Rabi box*, the signal is first downconverted to 40 MHz by mixing with an LO (red) at $f_q + 40$ MHz, which is itself generated by mixing another LO (orange) at $f_q + 70$ MHz with a continuous sine wave at 30 MHz generated by the AWG. The phase of this 30 MHz wave can be set arbitrarily and therefore allows to control the total phase shift α in the *Rabi box*. Then the fluorescence signal (now at low-frequency) is further amplified while spurious noise is tightly filtered out of a 25 MHz bandwidth. The resulting signal is finally upconverted back to f_q and goes through a variable attenuator allowing us to tune the total gain G_{R} of the *Rabi box*. In the *FM box*, the fluorescence signal is similarly first amplified and filtered tightly on a 2 MHz bandwidth at low frequency. It is then upconverted to $f_c + 100$ MHz (by mixing with the green LO), goes through a variable attenuator allowing to control the total gain G_{FM} and combined with a constant tone at the same frequency. This tone is obtained by mixing the LO (green) at $f_c + 170$ MHz with a continuous sine at 70 MHz generated by the AWG; its phase allows to control the phase β of the fluorescence signal quadrature that will be used to modulate the qubit frequency (see Sec. I F). The constant drive of the *Drift box* (see Fig. 1) is implemented by attenuating by 30 dB the same LO as the one that is used for mapping $\langle\sigma_x\rangle$ to $\langle\sigma_z\rangle$ during tomography, and hence shares the same phase reference as the final state tomography.

D. Electrical delays in the loop

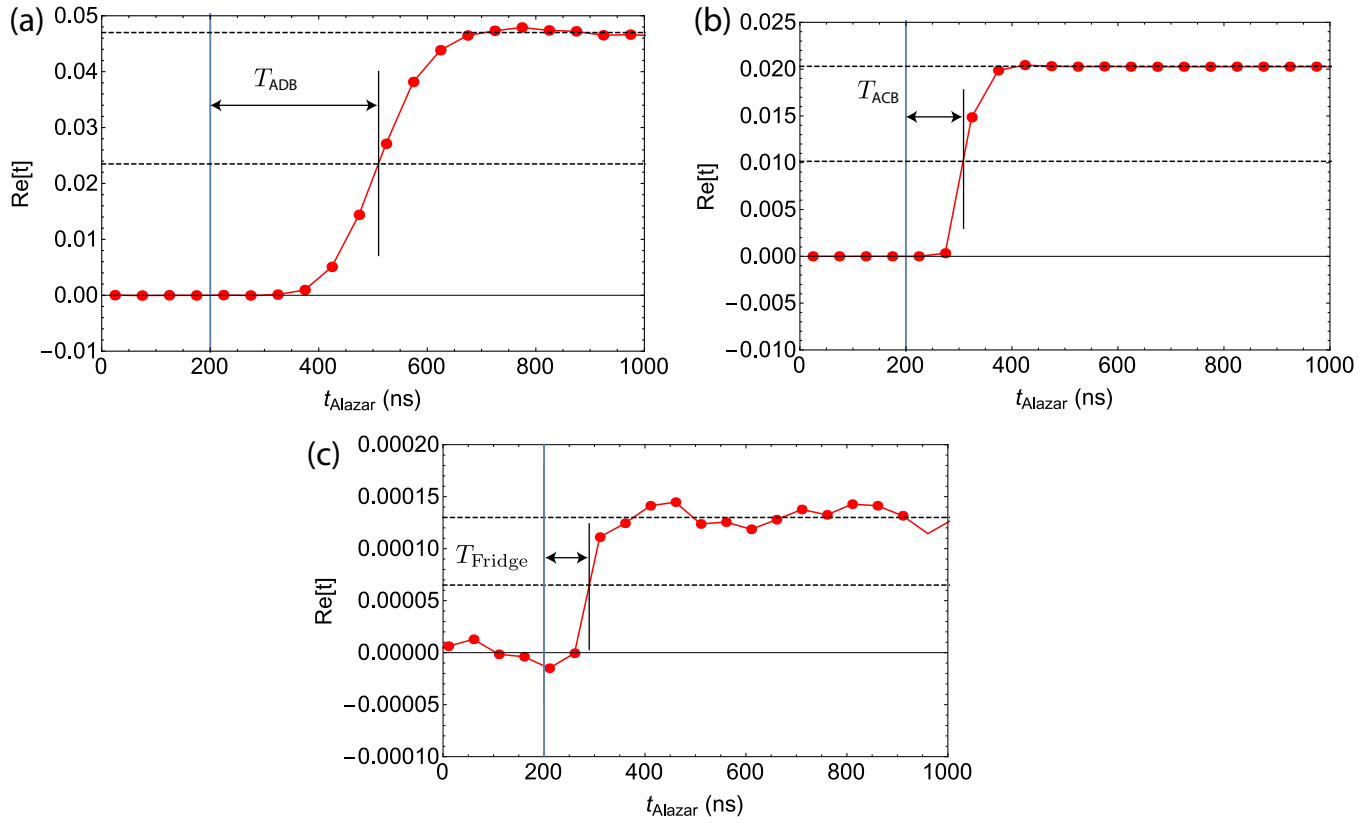

Figure S3: Transmitted signal from A to C on Fig. S2 through various parts of the circuit, for a square input signal triggered at t=200 ns. (a) through D (b) through C (c) from B to A through the refrigerator. The square signal is distorted by the finite detection bandwidth and the various bandpass filters along its propagation. The most heavily filtered path is *ADB*.

In order to measure the propagation time of the signal in the Rabi and FM boxes, we generate a square pulse at f_q,

send it through various parts of the circuit and measure it with the Alazar board. In Fig. S3a (resp. b, c), the time trace recorded by the board corresponds to a pulse starting at $t = 200$ ns and going from point A to point B through point D (resp. point C, and B-fridge-A) of Fig. S2. The arrival time of the pulse is taken at the middle of the rising edge since the square shape is distorted by various filters which induce group delays that must be taken into account. We obtain

$$\left\{ \begin{array}{rcll} T_{\rm Rabi} & = & T_{ACB} - T_{\rm meas} + T_{\rm fridge} - T'_{\rm meas} & = & 125 \text{ ns} \\ T_{\rm FM} & = & T_{ADB} - T_{\rm meas} + T_{\rm fridge} - T'_{\rm meas} - T_{\rm 2MHz} & = & 115 \text{ ns} \end{array} \right. , \tag{S4}$$

where we have subtracted the time $T_{\rm meas}$ (resp. $T'_{\rm meas}$) required by the square pulse to go from the AWG to point A (resp. B) and then from point B to the detector (resp. A to detector). We have also subtracted the group delay $T_{\rm 2MHz} = 210$ ns of the 2 MHz bandpass of the FM box since it will be explicitly taken into account in the Monte-Carlo simulations. Note that the JPC was turned off during the measurement of $T_{\rm fridge}$, so that its dynamics does not contribute to the measured delay.

E. Detection efficiency

The total measurement efficiency η of the relaxation channel that appears in Eqs. (1, S3) depends on both the probability that a relaxation event triggers the emission of a photon and on our capacity to detect this photon.

The total qubit decay rate γ_1 includes the effect of spurious and unknown relaxation processes beyond fluorescence. We call $\eta_{\rm rad}$ the fraction of relaxation events that lead to the emission of a photon. It is defined by the associated Purcell induced relaxation rate $\gamma_{\rm Purcell} = \eta_{\rm rad}\ \gamma_1$. This rate depends on the electromagnetic environment of the system as [32] $\gamma_{\rm Purcell} = \frac{2{\rm Re}[Y(f_q)]}{{\rm Im}[Y'(f_q)]}$, where Y is the admittance seen by the Josephson junction of the transmon. However, this rate cannot be precisely estimated in our experiment due to the uncalibrated impedance of the transmission lines probing the cavity. Note that a simple model including a single cavity mode coupled to an ohmic environment [32] does not work here since it yields an estimated value $\gamma_{\rm Purcell} = \kappa\frac{\chi}{2\alpha} \simeq (1\ \mu{\rm s})^{-1}$, which is larger than the measured qubit decay rate $\gamma_1 = (4.7\ \mu{\rm s})^{-1}$.

Note that the coupling $\kappa_{\rm out}$ to the output line was intentionally chosen to dominate the one of the input line and the cavity internal losses in order to maximize the collection efficiency $\eta_{\rm coll}$ on the output line, where the heterodyne detection takes place. Indeed, for perfect transmission lines (constant impedance) one would get $\eta_{\rm coll} \simeq \frac{\kappa_{\rm out}}{\kappa}$.

The total detection efficiency η is thus reduced by the unknown factor $\eta_{\rm rad}\eta_{\rm coll}$ compared to the sole detector efficiency $\eta_{\rm detec}$ so that

$$\eta = \eta_{\rm rad} \times \eta_{\rm coll} \times \eta_{\rm detec}. \tag{S5}$$

In order to estimate the total measurement efficiency η, we compare the mean value of the fluorescence signal to the amplitude of its fluctuations. The former is given by Eq. (S3) while the latter, according to Eq. (1), has a standard deviation $\sigma = \lambda\sqrt{T}$ for $T = 5\ \mu{\rm s} \gg 1/2\pi B$ (where $B = 3.3$ MHz is the detection bandwidth set by the JPC). Fig. S4 shows the 2D histogram of around 3000 measurements of $(V_{I,{\rm int}}, V_{Q,{\rm int}})$ for the qubit prepared in $|g\rangle$ from which we extract σ. The point A furthermore shows the measured value of $(\overline{V_{I,{\rm int}}}, \overline{V_{Q,{\rm int}}})$ when the qubit is prepared in $(|e\rangle + |g\rangle)/\sqrt{2}$. We then obtain $\eta = 2\left(\frac{\overline{V_{I,{\rm int}}}}{1-e^{-\gamma_2 T}}\right)^2 \frac{\gamma_2^2}{\gamma_1}\frac{T}{\sigma^2} = 35 \pm 1\ \%$.

F. Frequency Modulation of the qubit

Following Gambetta *et al.* in [37], when the cavity is driven with a detuned microwave at $f_c + \Delta$ of amplitude $\epsilon(t)$, the qubit resonance frequency is shifted by $\delta f = w/2\pi$ (AC Stark shift) and its coherences are damped with an extra dephasing rate γ_m (measurement induced dephasing), which are given by

$$\left\{ \begin{array}{rcl} \gamma_m(t)/2\pi & = & \chi\ {\rm Im}[\alpha_e(t)\alpha_g(t)^*] \\ \delta f(t) & = & \chi\ {\rm Re}[\alpha_e(t)\alpha_g(t)^*] \end{array} \right. , \tag{S6}$$

where $\alpha_{g,e}$ are the coherent states developing in the cavity when the qubit remains in $|g\rangle$ and $|e\rangle$. They are governed by the following equations of motion

$$\left\{ \begin{array}{rcl} \dot{\alpha_g}(t) & = & 2\pi i(\Delta - \frac{\chi}{2})\alpha_g(t) - \frac{\kappa}{2}\alpha_g(t) + \epsilon(t) \\ \dot{\alpha_e}(t) & = & 2\pi i(\Delta + \frac{\chi}{2})\alpha_e(t) - \frac{\kappa}{2}\alpha_e(t) + \epsilon(t) \end{array} \right. . \tag{S7}$$

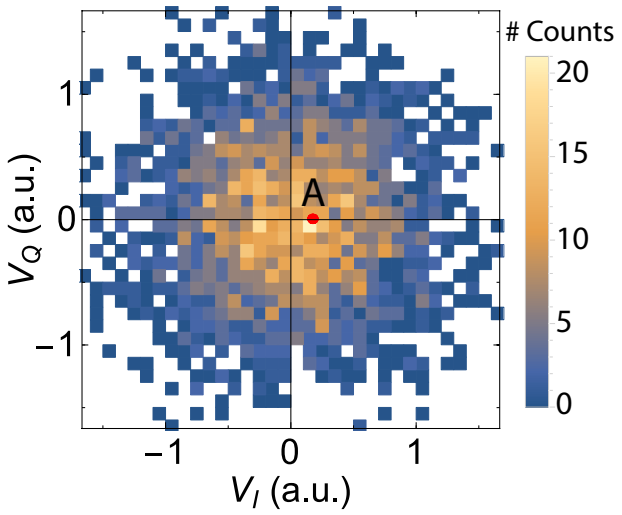

Figure S4: Density plot of the histogram of measured values of the two quadratures V_I, V_Q of the fluorescence field for a set of 2880 independent samples where the qubit remains at thermal equilibrium. The point A indicates the average value of another set of measurements corresponding to a qubit initially prepared in $(|e\rangle + |g\rangle)/\sqrt{2}$.

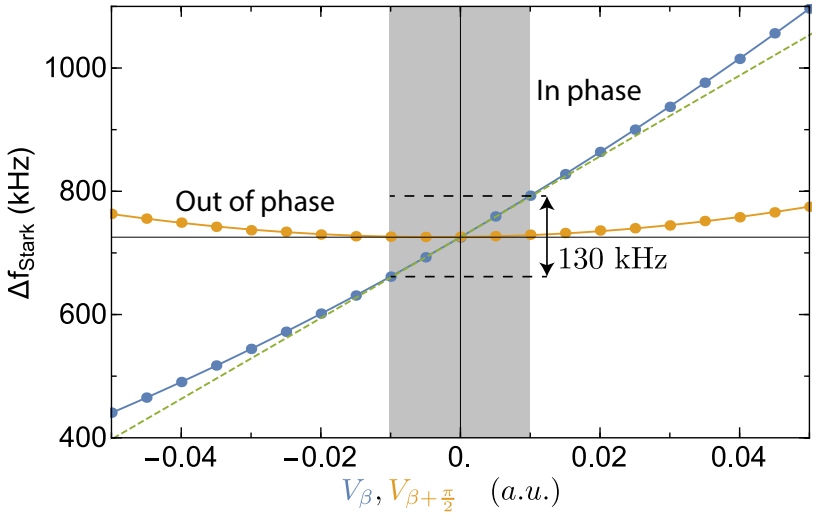

Figure S5: Measured value of the ac-Stark shift of the qubit frequency as a function of a signal in phase (blue dots) or out of phase (yellow dots) with the constant microwave drive of large amplitude ϵ_0 and phase β.The horizontal scale is in arbitrary units, but the gray region delimits the typical values taken by the output signals in the experiment. Solid lines correspond to the quadratic fit used in the simulations.

If the amplitude $\epsilon(t)$ varies much more slowly than the detuning time Δ^{-1}, the cavity states $\alpha_{g,e}$ take at each time the value corresponding to the stationary solution of Eq. (S7) for the current value of ϵ:

$$\begin{cases} \alpha_g(t) \simeq \alpha_{g,\mathrm{stat}}(t) = \frac{2\epsilon(t)}{\kappa - 2i\pi(2\Delta - \chi)} \\ \alpha_e(t) \simeq \alpha_{e,\mathrm{stat}}(t) = \frac{2\epsilon(t)}{\kappa - 2i\pi(2\Delta + \chi)} \end{cases} . \tag{S8}$$

In this case, one can check that $\frac{\gamma_m}{\delta f} \underset{\Delta\to\infty}{\to} 0$. A large enough Δ thus allows to modulate the qubit frequency without inducing detrimental extra dephasing. One also sees that the qubit frequency shift $\delta f(t)$ is proportional to $|\epsilon(t)|^2$. However, the feedback law requires δf to depend linearly on a single quadrature $V_\beta(t) = V_I(t)\cos\beta + V_Q(t)\sin\beta$ of the fluorescence field (see the "FM box" in Fig. 1). To achieve this, the fluorescence signal is combined (after upconversion to $f_c + \Delta$) with a constant microwave at $f_c + \Delta$ of large amplitude ϵ_0 and phase β. Following Eqs. (S6) and (S8), the

resulting shift of the qubit resonance frequency is

$$w(t)/2\pi = \chi \mathrm{Re}[\alpha_{e,\mathrm{stat}}(t)\alpha_{g,\mathrm{stat}}(t)^*] = R'G'^2|\epsilon_0 e^{i\beta} + G(V_I(t) + iV_Q(t))|^2 = R\left(\epsilon_0^2 + 2G\epsilon_0 V_\beta(t) + \underbrace{G^2\left(V_\beta^2 + V_{\beta+\frac{\pi}{2}}^2\right)}_{o(\epsilon_0)}\right), \tag{S9}$$

where $R = R'G'^2 = \mathrm{Re}[\frac{4\chi}{(\kappa-2i\pi(\chi-2\Delta))(\kappa-2i\pi(\chi+2\Delta))}] \times G'^2$ and G (resp. G') accounts for the overall gain experienced by the feedback signal before (resp. after) it is combined with the constant microwave.
We argue that the first order approximation leading to the last equality of Eq. (S9) is valid since the frequency offset $R\epsilon_0^2 = 810$ kHz is much higher than the fluctuating term $2RG\epsilon_0 V_\beta(t)$whose standard deviation is $G_{\mathrm{FM}}\sqrt{B_f}/2\pi \leq \sqrt{\gamma_1 B_f/8\eta}/2\pi \simeq 65$ kHz. This statement is directly verified in Fig. S5, which shows measured values of the Stark shift as a function of the amplitude of a signal sent in phase (blue points) or out-of-phase (orange points) with the constant microwave. It appears that the Stark shift is to a very good accuracy linear in the in-phase signal (that is V_β) and independent of the out-of-phase signal (that is $V_{\beta+\pi/2}$) on the typical range of Stark shifts required by the feedback law (gray range in Fig. S5).

II. CLOSED-LOOP MASTER EQUATION

A. Derivation and theoretical analysis

1. *Preliminary: the SISO case*

For simplicity, we first consider the case of a Single Input Single Output (SISO) Markovian feedback following [5, 6, 24]. We also neglect the pure dephasing of the qubit so that the only decoherence channel is a relaxation channel monitored by homodyne detection with efficiency η as in [4]. In the absence of feedback, the system is governed by the following Stochastic Master Equation (SME)[2]

$$\rho(t+\mathrm{d}t) - \rho(t) = -\frac{i}{\hbar}\mathrm{d}t[H,\rho(t)] + \gamma_1 \mathrm{d}t\mathcal{D}[\sigma_-]\rho(t) + \sqrt{\eta\gamma_1}\mathrm{d}W_t\mathcal{M}[\sigma_-]\rho(t), \tag{S10}$$

with damping and measurement super operators $\mathcal{D}$ and $\mathcal{M}$ defined by

$$\left\{\begin{array}{rcl} \mathcal{D}[L]\rho &=& L\rho L^\dagger - \frac{1}{2}L^\dagger L\rho - \frac{1}{2}\rho L^\dagger L \\ \mathcal{M}[c]\rho &=& \big((c-\langle c\rangle)\rho + \rho(c^\dagger - \langle c^\dagger\rangle)\big) \end{array}\right. . \tag{S11}$$

The output signal V_I verifies (note that η is replaced by 2η in Eq. (1) in case of homodyne detection)

$$V_I\mathrm{d}t = \sqrt{\eta\gamma_1}\langle\sigma_x\rangle\mathrm{d}t + \mathrm{d}W_t. \tag{S12}$$

The controller associated with a SISO Markovian feedback (similar to the "boxes" of Fig. 1) simplifies into

$$u(t) = g \times V_I\,, \tag{S13}$$

where g is a constant scalar gain. The signal $u(t)$ modulates the strength of a control Hamiltonian which we call $\hbar\sigma_1$ (typically $\sigma_1 = \sigma_x$, σ_y or σ_Z for rotations around the axes of the Bloch sphere; the factor $\hbar$ is introduced to simplify notations below), such that the actual feedback action is given by $H_1(t) = \hbar g \times V_I\,\sigma_1$. We also possibly add a tailored constant term to the open-loop Hamiltonian H, modifying it into H_0.

The noise signal W_t is singular, since its variation during a time step $\mathrm{d}t$ is of order $\sqrt{\mathrm{d}t}$ and thus much larger than the time step $\mathrm{d}t$ itself. Therefore, we would not obtain the correct closed-loop evolution if we simply replace H by $H_0 + H_1(t)$ in Eq. (S10). Indeed due to the singular nature of W_t, the dominant term in the closed-loop evolution, as we take the limit $\mathrm{d}t \to 0$, depends on the order of infinitesimal operations involving W_t. The SME (S10) is a model in the sense of Itô, where preserving the physical causality simply corresponds to taking the order of operations: first apply the open-loop evolution (with Hamiltonian H_0) from t to $t+\mathrm{d}t$, and then use the measurement record V_I to apply the unitary $e^{-\frac{i}{\hbar}H_1(t)}$. The closed-loop evolution of ρ thus reads

$$\begin{array}{l}\rho(t+\mathrm{d}t) = \\ \quad e^{-\frac{i}{\hbar}H_1(t)\mathrm{d}t}\Big\{\rho(t) - \frac{i}{\hbar}\mathrm{d}t[H_0,\rho] + \gamma_1\mathrm{d}t\mathcal{D}[\sigma_-]\rho + \sqrt{\eta\gamma_1}\mathrm{d}W_t\mathcal{M}[\sigma_-]\rho(t)\Big\}e^{+\frac{i}{\hbar}H_1(t)\mathrm{d}t}.\end{array} \tag{S14}$$

We now simplify this formula using Itô rules, which state that $\overline{\mathrm{d}W_t} = 0$ and $\overline{\mathrm{d}W_t^2} = \mathrm{d}t$. Via the Baker-Campbell-Hausdorff formula

$$e^A B e^{-A} = B + [A, B] + [A, [A, B]]/2 + O(||A||^3) \tag{S15}$$

with

$$\begin{cases} A &= -ig\sigma_1(\sqrt{\eta\gamma_1}\langle\sigma_x\rangle\mathrm{d}t + \mathrm{d}W_t) \\ B &= \rho(t) - \frac{i}{\hbar}\mathrm{d}t\,[H_0, \rho] + \gamma_1\mathrm{d}t\,\mathcal{D}[\sigma_-]\rho + 2\sqrt{\eta\gamma_1}\mathrm{d}W_t\,\mathcal{M}[\sigma_-]\rho \end{cases} \tag{S16}$$

and neglecting terms of order $O(\mathrm{d}t^{3/2})$ we get the effective master equation

$$\begin{aligned} \rho(t+\mathrm{d}t) - \rho(t) &= -i\mathrm{d}t[\tfrac{H_0}{\hbar} + \tfrac{g\sqrt{\eta\gamma_1}}{2}(\sigma_-\sigma_1 + \sigma_1\sigma_+), \rho(t)] \\ &\quad + \mathrm{d}t\mathcal{D}[L_1]\rho(t) + 2\sqrt{\eta}\mathrm{d}W_t\mathcal{M}[L_1]\rho(t) \\ &\quad + \mathrm{d}t\mathcal{D}[L_2]\rho(t) + 2\sqrt{1-\eta}\mathrm{d}W_t\mathcal{M}[L_2]\rho(t), \end{aligned} \tag{S17}$$

with

$$\begin{cases} L_1 &= \sqrt{\gamma_1}\sigma_- - ig\sqrt{\eta}\sigma_1 \\ L_2 &= -i\sqrt{1-\eta}g\sigma_1 \end{cases}. \tag{S18}$$

Note that a constant drift $H_{\mathrm{drift}} = \frac{g\sqrt{\eta\gamma_1}}{2}(\sigma_-\sigma_1 + \sigma_1\sigma_+)$ has appeared in the effective hamiltonian. Compensating this term, or adjusting it to a given value, is the reason why we have introduced the modified constant drive H_0. Such constant drives are necessary to stabilize an arbitrary state of the Bloch sphere (see Eq. (S25)).

More importantly, for efficiency $\eta = 1$, the effect of the feedback is thus to modify the initial damping operator $\sqrt{\gamma_1}\sigma_-$ into an effective damping operator $\sqrt{\gamma_1}\sigma_- - ig\sigma_1$. Appropriate choices of $g\sigma_1$ hence allow to engineer the dissipation in order to stabilize other states than $|g\rangle$. This has been studied in detail by the authors of [5, 6, 24], see also e.g. [38].
For instance, when choosing $\sigma_1 = \sigma_y$ and $g = -2\sqrt{\gamma_1}$ so that $L_1 = \sqrt{\gamma_1}\sigma_+$, dissipation now causes the qubit to relax toward the $|e\rangle$ state. This feedback thus stabilizes $|e\rangle$ much like the open-loop system stabilizes $|g\rangle$.

For $\eta < 1$, a new damping operator $L_2 = -i\sqrt{1-\eta}g\sigma_1$ appears, limiting the fidelity of the stabilized state to the target state.

In this section, we have described a continuous, Markovian, feedback loop in the SISO (single-input, single-output) regime. In practice, it describes a continuous feedback based on a homodyne detection. In the next section, we generalize the results to MIMO, which can model feedback using heterodyne detection, such as in the present experiment.

Before going on, let us comment on two straightforward variations on the effective SME (S17).

- First, when the initial master equation describes additional but unmonitored dissipative channels (e.g. dephasing) these can just be added to (S17) exactly like in the initial SME. Indeed the feedback introduces an effect by correlation between the noise introduced in a given damping channel and the *same* noise being fed back by the controller; the other channels remain unaffected in the SME.
- Second and more straightforwardly, in the present experiment we are concerned with the average predicted stabilization, so that the relevant part of (S17) is obtained by leaving out the two so-called "actuation terms", i.e. those proportional to $\mathrm{d}W_t$.

2. MIMO Markovian feedback

We now turn to the case of the present experiment, in which we perform heterodyne detection of the fluorescence (2 inputs) and control the qubit by rotating its state around the three axis of the Bloch sphere (3 outputs) as shown in Fig S6. In the absence of feedback, the system is governed by the following Stochastic Master Equation (SME)[2]

$$\rho(t+\mathrm{d}t) - \rho(t) = -\frac{i}{\hbar}\mathrm{d}t[H_0, \rho(t)] + \gamma_1\mathrm{d}t\mathcal{D}[\sigma_-]\rho(t) + \sqrt{\frac{\eta\gamma_1}{2}}\mathrm{d}W_{I,t}\mathcal{M}[\sigma_-]\rho(t) + \sqrt{\frac{\eta\gamma_1}{2}}\mathrm{d}W_{Q,t}\mathcal{M}[i\sigma_-]\rho(t), \tag{S19}$$

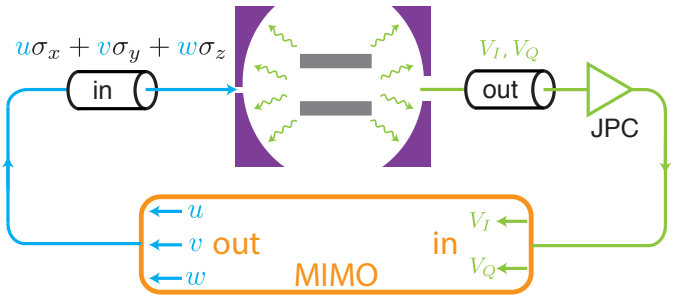

Figure S6: Scheme of the Multiple-Input-Multiple-Output feedback. The output of the measurement setup feeds the input of the MIMO controller while the output of the latter feeds the control signals at the input of the refrigerator.

where $W_{I,t}$ and $W_{Q,t}$ are two independent Wiener processes. The Multi Input Multi Output (MIMO) gain, imposing how each input influences each output (only the non constant parts are considered here), thus consists of a 2-by-3 matrix G

$$\begin{pmatrix} \delta u(t) \\ \delta v(t) \\ w(t) \end{pmatrix} = G \times \begin{pmatrix} V_{I_t} \\ V_{Q_t} \end{pmatrix} . \tag{S20}$$

The derivation of the closed-loop master equation for MIMO systems is derived by Chia and Wiseman in [14]. It can be obtained with exactly the same computations as in the previous section, just involving a somewhat more involved control action via $H_1(t)$. One still applies the infinitesimal unitary motion corresponding to the feedback action *after* the associated open-loop evolution. In the computations related to applying Baker-Campbell-Hausdorff formula, the equivalent of A in Eq.(S16) contains one noise term $\mathrm{d}W_t^{(j)}$ per input channel $j = 1, 2, ...$, and Itô calculus must be applied with the rules $\mathrm{d}W_t^{(j)}\mathrm{d}W_t^{(j')} = 0$ if $j \neq j'$ (while for $j = j'$ we still have the rule $(\mathrm{d}W_t^{(j)})^2 = \mathrm{d}t$). This yields a new SME that is a generalization of the SISO case (S17).

The drift in the effective hamiltonian reads

$$H_{\mathrm{drift}} = \frac{\hbar}{2}\sqrt{\frac{\eta\gamma_1}{2}} \sum_{\alpha\in\{X,Y,Z\}} G_{\alpha,I}(\sigma_\alpha\sigma_- + \sigma_+\sigma_\alpha) + G_{\alpha,Q}(i\sigma_\alpha\sigma_- - i\sigma_+\sigma_\alpha) , \tag{S21}$$

where, for compactness, we call G_α the rows of G, with the correspondence $1 \leftrightarrow X$, $2 \leftrightarrow Y$ and $3 \leftrightarrow Z$. As for the two initial damping operators $\sqrt{\frac{\gamma_1}{2}}\sigma_-$ and $\sqrt{\frac{\gamma_1}{2}}i\sigma_-$ of the heterodyne measurement channels, they lead to four effective damping operators

$$\begin{cases} L_{I,1} &= \sqrt{\frac{\gamma_1}{2}}\sigma_- - i\sqrt{\eta} \sum\limits_{\alpha\in\{X,Y,Z\}} G_{\alpha,I}\sigma_\alpha \\ L_{Q,1} &= i\sqrt{\frac{\gamma_1}{2}}\sigma_- - i\sqrt{\eta} \sum\limits_{\alpha\in\{X,Y,Z\}} G_{\alpha,Q}\sigma_\alpha \\ L_{I,2} &= -i\sqrt{1-\eta} \sum\limits_{\alpha\in\{X,Y,Z\}} G_{\alpha,I}\sigma_\alpha \\ L_{Q,2} &= -i\sqrt{1-\eta} \sum\limits_{\alpha\in\{X,Y,Z\}} G_{\alpha,Q}\sigma_\alpha \end{cases} . \tag{S22}$$

With these notations, the master equation becomes

$$\begin{aligned} \rho(t+\mathrm{d}t) - \rho(t) \;=\; & -\tfrac{i}{\hbar}\mathrm{d}t[H_0 + H_{\mathrm{drift}}, \rho(t)] \\ & +\mathrm{d}t\mathcal{D}[L_{I,1}]\rho(t) + \mathrm{d}t\mathcal{D}[L_{I,2}]\rho(t) \\ & +\mathrm{d}t\mathcal{D}[L_{Q,1}]\rho(t) + \mathrm{d}t\mathcal{D}[L_{Q,2}]\rho(t) \\ & +\mathrm{d}t\mathcal{D}[\sqrt{\tfrac{\gamma_\phi}{2}}\sigma_z]\rho(t) \end{aligned} \tag{S23}$$

where we have added an unmonitored dephasing term, and dropped the actuation terms in $\mathrm{d}W$ which are not used in the experiment.

3. Arbitrary state stabilization for $\eta = 1$

We now want to stabilize the pure state $\rho_{\text{target}} = |\psi_{\theta,\frac{\pi}{2}}\rangle\langle\psi_{\theta,\frac{\pi}{2}}| = \frac{1}{2}(\mathbf{1} + \sin\theta\sigma_y + \cos\theta\sigma_z)$, see Fig. 3c. As mentioned in the main text, it can be generalized to any state of the Bloch sphere by changing its longitude using the knob of the angle β in the FM box.

We first consider the case $\gamma_\phi = 0$ and $\eta = 1$, where analysis is greatly simplified by the fact that $L_{I,2}$ and $L_{Q,2}$ are zero. In principle, the state can be kept pure as we lose no information to the environment.

Much like the ground state $|g\rangle\langle g|$ is stabilized by $\mathcal{D}(\sigma_-)$ with $\sigma_- = \sigma_x/2 - i\sigma_y/2$, the state ρ_{target} would be stabilized with $L_{I,1} = \sigma_x/2 - i(\cos\theta\sigma_y - \sin\theta\sigma_z)/2$. It is clear that such $L_{I,1}$ can be obtained, for any value of θ, with an appropriate choice of the $G_{\alpha,I}$.

For $L_{Q,1}$ the same strategy is not possible for all θ, but we can get $L_{Q,1} = U_\theta^\dagger\,(\beta_\theta\sigma_- + \beta'_\theta\sigma_z)\,U_\theta$ for some real β_θ and β'_θ, where U_θ is a unitary matrix on the qubit Hilbert space satisfying $U_\theta^\dagger\,|g\rangle\langle g|\,U_\theta = \rho_{\text{target}}$. Writing down $L_{Q,1}\rho L_{Q,1}^\dagger$ and $\frac{1}{2}L_{Q,1}^\dagger L_{Q,1}\rho$ in the basis rotated by U_θ we obtain respectively

$$(\beta_\theta\sigma_- + \beta'_\theta\sigma_z)\tilde{\rho}(\beta_\theta\sigma_+ + \beta'_\theta\sigma_z) \quad \text{and} \quad \tfrac{1}{2}(\beta_\theta^2|e\rangle\langle e| + \beta_\theta\beta'_\theta\sigma_x + (\beta'_\theta)^2\mathbf{1})\tilde{\rho}\,,$$

where $\tilde{\rho} = U_\theta\rho U_\theta^\dagger$. In particular, at $\tilde{\rho} = |g\rangle\langle g|$, we have

$$U_\theta\left(L_{Q,1}\rho L_{Q,1}^\dagger - \tfrac{1}{2}L_{Q,1}^\dagger L_{Q,1}\rho - \tfrac{1}{2}\rho L_{Q,1}^\dagger L_{Q,1}\right)U_\theta^\dagger \;= -\tfrac{\beta'_\theta\beta_\theta}{2}(|e\rangle\langle g|\tilde{\rho} + \tilde{\rho}|g\rangle\langle e|) \tag{S24}$$

But for $\tilde{\rho} = |g\rangle\langle g|$ we have as well $-i[\sigma_y, \tilde{\rho}] = |e\rangle\langle g|\tilde{\rho} + \tilde{\rho}|g\rangle\langle e|$, so the effect of having $\beta'_\theta \neq 0$ is, *on the target state and only there*, equivalent to having a Hamiltonian in σ_y on $\tilde{\rho}$. Therefore the effect of $\beta'_\theta \neq 0$ on the target state can be compensated by adjusting H_0 such that $H_0 + H_{\text{drift}}$ is the appropriate multiple of $U_\theta^\dagger\sigma_y U_\theta$.

This procedure leads to the following control parameters:

$$\begin{pmatrix} u(t) \\ v(t) \\ w(t) \end{pmatrix} = \begin{pmatrix} 0 & \sqrt{\frac{\gamma_1}{8\eta}}(1+\cos\theta) \\ -\sqrt{\frac{\gamma_1}{8\eta}}(1+\cos\theta) & 0 \\ \sqrt{\frac{\gamma_1}{8\eta}}\sin\theta & 0 \end{pmatrix} \times \begin{pmatrix} V_{I_t} \\ V_{Q_t} \end{pmatrix} \quad \text{and} \quad H_0 = \frac{\hbar\gamma_1}{8}(1 - \cos\theta/\eta)\sin\theta\;\sigma_x \tag{S25}$$

In Eq. (S25), the first term of H_0 compensates for $H_{\text{drift}} = -\hbar\frac{\gamma_1\sin\theta}{8}\;\sigma_x$ whereas the second term is necessary to compensate for the just discussed side-effect of $L_{Q,1}$. We can then show that ρ_{target} is a stationary state of Eq. (S23) for $\eta = 1$, meaning that $-\frac{i}{\hbar}\mathrm{d}t[H_0 + H_{\text{drift}}, \rho_{\text{target}}] + \mathrm{d}t\mathcal{D}[L_{I,1}]\rho_{\text{target}} + \mathrm{d}t\mathcal{D}[L_{Q,1}]\rho_{\text{target}} = 0$. For $\eta < 1$, we still have $L_{I,1} = -i\,U_\theta^\dagger\,\sigma_-\,U_\theta$ and $L_{Q,1} = U_\theta^\dagger\,(\beta_\theta\sigma_- + \beta'_\theta\sigma_z)\,U_\theta$, but the non-zero damping operators $L_{I,2}$ and $L_{Q,2}$ limit the fidelity of the stabilized state to the target state. The controller (S25) is the one implemented in the experiment but is not optimized to maximize the fidelity to the target state for $\eta < 1$. We will describe an optimal controller in the next subsection, for the moment (S25) is to be considered with $\eta = 1$.

Having thus ensured that the target state is kept invariant by the closed-loop dynamics, it remains to check that all the other states of the Bloch sphere indeed get attracted towards the target. Indeed, when considering, for example, a SISO feedback loop with $\sigma_1 = \sigma_y$ and $g = -\sqrt{\gamma_1}$, corresponding to homodyne detection of the fluorescence, one gets an effective damping operator $L_1 = \sqrt{\gamma_1}\sigma_x$. Then for $\eta = 1$, although a system initially prepared in the state e.g. $|+x\rangle$ would not move in an ideal world, $|+x\rangle$ is not attractive: if some small noise perturbs the initial $|+x\rangle$, nothing will attract the state back to this target. The goal of stabilization, or unconditional preparation, is precisely to ensure that any (initial or perturbed) state is attracted back towards the target. In our system, thanks to the presence of $L_{I,1}$ which attracts all states to the target, we have good hope to satisfy this property. However, as the sum of two stable linear operators is not necessarily stable, we must check how the system behaves under the combined effects of $L_{I,1}, L_{Q,1}$ and $H_{\text{drift}} + H_0$.

For this we translate the master equation of the type

$$\frac{\mathrm{d}}{\mathrm{d}t}\rho(t) \;=\; -\frac{i}{\hbar}[\tfrac{\hbar\beta\beta'}{2}\sigma_y\,,\,\rho(t)] + \mathcal{D}[\sigma_-]\rho(t) + \mathcal{D}[\beta\sigma_- + \beta'\sigma_z]\rho(t)\,, \tag{S26}$$

resulting from a coordinate change by U_θ on (S23) with appropriate tuning, into Bloch coordinates. This yields:

$$\tfrac{\mathrm{d}}{\mathrm{d}t}\begin{pmatrix} x(t) \\ y(t) \\ z(t) \end{pmatrix} = \begin{pmatrix} -x/2 + \beta\beta' + \beta\beta'\,(1+z) - (2\beta'^2 + \beta^2/2)x + \beta\beta'\,z \\ -y/2 - (2\beta'^2 + \beta^2/2)y \\ -(1+z) + \beta\beta'\,x - \beta^2(1+z) - \beta\beta'\,x \end{pmatrix}.$$

From this expression it is easy to conclude. Indeed for all values of β, β', the y coordinate converges to 0 and is decoupled from the others; the z coordinate converges to -1 independently of the other coordinates; and the x coordinate, although influenced by the decaying z, also stably converges to zero. This demonstrates that every state is attracted, in the usual basis, towards $U_\theta^\dagger|g\rangle$, which is the target state.

4. Targeting arbitrary states for $\eta < 1$

We have included the parameter η in (S25) to suggest how the tuning might be adapted for $\eta < 1$. Indeed with this tuning, $L_{I,1}$ and $L_{Q,1}$ are independent of η. Thus if we neglect the effect of $L_{I,2}$ and $L_{Q,2}$, the closed-loop system would still stabilize the target state perfectly for $\eta < 1$. One might then expect that, at least when η is close to 1, the dynamics is dominated by $L_{I,1}, L_{Q,1}, H_0 + H_{\rm drift}$ which attract the state to the target, while the small perturbation induced by $L_{I,2}$ and $L_{Q,2}$ limits the preparation fidelity. Pure dephasing and finite feedback delay also limit this fidelity. All these effects will be taken into account in the simulations described in the following section. In that case, the markovian controller defined in Eq. (S25) is *not* optimized to get as high a preparation fidelity to $\rho_{\rm target}$ as possible. In the following paragraphs we provide an analysis that includes $L_{I,2}$ and $L_{Q,2}$

It is not too difficult to analytically compute the optimal tuning parameters for (S23) when $\eta < 1$. For this we first translate (S23) into Bloch coordinates for general feedback parameters G and H_0. This gives an equation of the type

$$\frac{d}{\mathrm{d}t}\begin{pmatrix} x(t) \\ y(t) \\ z(t) \end{pmatrix} = A \begin{pmatrix} x(t) \\ y(t) \\ z(t) \end{pmatrix} + B \tag{S27}$$

with A a 3-by-3 matrix and B a 3-component vector, both composed of second-order polynomials in the control parameters. We then fix a target value for θ, impose $y = z\tan(\theta)$ and require the target to satisfy $A\,(\,x\,;\,y\,;\,z\,) = -B$ in order to remain invariant. The purest state achievable at colatitude θ on the Bloch sphere is then obtained by maximizing z over all control parameters, subject to the constraints of the previous sentence. The variable x luckily plays a minor role and a few smart combinations of the variables allow to reduce the constrained optimization problem to solving second-order polynomials. This allows to get the following optimal tuning parameters, for $\gamma_\phi = 0$:

$$\begin{pmatrix} u(t) \\ v(t) \\ w(t) \end{pmatrix} = \begin{pmatrix} 0 & \sqrt{\frac{\gamma_1}{8\eta}}(1+c_f) \\ -\sqrt{\frac{\gamma_1}{8\eta}}(1+c_f) & 0 \\ \sqrt{\frac{\gamma_1}{8\eta}}s_f & 0 \end{pmatrix} \times \begin{pmatrix} V_{I_t} \\ V_{Q_t} \end{pmatrix} \quad \text{where} \quad \left\{ \begin{array}{rcl} f &=& (1-\eta)\frac{1-\cos^2\theta}{1+\cos^2\theta} \\ c_f &=& \cos\theta\sqrt{1-f^2} - f \\ s_f &=& \sin\theta\sqrt{1-f^2} + 2f/\tan\theta \end{array} \right. , \tag{S28}$$

and

$$H_0 = \left(\frac{\hbar\gamma_1}{8} s_f (1 - \cos\theta/\eta)\sin\theta - \frac{\hbar\gamma_1}{8\eta} \left(\frac{(1+c_f^2)(2+3\sin^2\theta) - (1+\cos^2\theta)s_f^2 - 4}{2\cos\theta\sin\theta} + 3c_f(1-\eta)\tan\theta \right) \right) \sigma_x \,. \tag{S29}$$

We finally estimate the exponential rate at which the state converges to the equilibrium with a so-called Lyapunov technique from control theory. Denoting by $\Delta s(t) \in \mathbb{R}^3$ the difference between the Bloch vectors of the actual state vector and of the equilibrium, one computes by simple evaluation that under the dynamics given by (S27) we have

$$\frac{d}{\mathrm{d}t}||\Delta s||^2 \leq -||\Delta s||^2/T_1$$

for any parameter choice according to (S28) or (S25), and for any η. This gives the convergence rate reported in the main paper. If desired, for any given values of θ, η, a more accurate convergence rate can be obtained by numerically computing the eigenvalues of the matrix A in (S27).

One can check as above that all the states indeed get attracted to the equilibrium. Indeed for any values of the tuning parameters and any η, the linear system $\frac{\mathrm{d}}{\mathrm{d}t}s = A\,s$ with $s \in \mathbb{R}^3$ and the matrix A defined in (S27), is ensured to converge to $s = 0$. (This more general result covers the case worked out above for $\eta = 1$.) One quick way to prove this is with a so-called Lyapunov function, e.g. showing that $\frac{\mathrm{d}}{\mathrm{d}t}(s^\dagger\, s)$ is always strictly negative except when $s = 0$.

The associated best achievable radius $R_{\rm opt}$ in each direction is given by

$$\frac{1}{R_{\rm opt}} = \frac{1}{\eta}\sqrt{1-f^2} + \frac{2\cos\theta}{1+\cos^2\theta}\left(\frac{1}{\eta} - 1\right) .$$

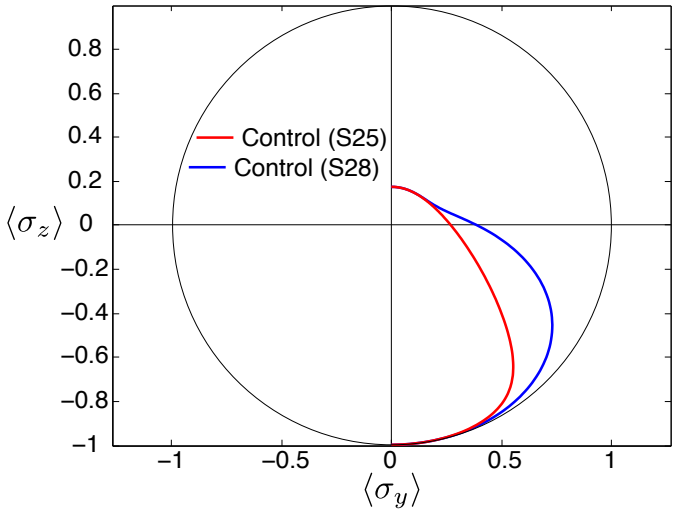

Figure S7: Spanned ensemble of states in the Bloch sphere that are stabilized by Markovian feedback aiming at targets of the form $|\psi_{\theta,\pi/2}\rangle$, for $\eta = 0.35$. The curves correspond to feedback laws proposed in Control (S25) and used in the experiment (i.e. neglecting the effect of $L_{I,2}$ and $L_{Q,2}$) for the red line and in Control (S28) (i.e. the optimal one for $\gamma_\phi = 0$) for blue.

It is depicted on Fig. S7 for a value $\eta = 0.35$, and compared to the theoretical radius achievable when tuning the controller according to (S25). The predictions for targets close to $|g\rangle$ and $|e\rangle$ are similar. For target states closer to the equator of the Bloch sphere, there is a significant difference, showing that the controller (S25), which is used in the experiment, is not optimal. We did not try to implement the optimal controller (S28) but the fidelity of the stabilized states seem to be anyway limited by another mechanism (see next section).

III. SIMULATIONS

A. Limitations of the calibration procedure for the gain

Let us recall how G_R and $G_{\rm FM}$ are set in the experiment. The gain of the Rabi box G_R is first varied while the FM box is turned off, and the resulting stabilized states are fitted to the results of numerical simulations with a scaling factor accounting for the attenuation of the lines (see Fig. 2). The experimental data is well reproduced, and we can thus determine the loop gain (in practice set by the a variable attenuator on Fig. S2) for which $G_R = \sqrt{\frac{\gamma_1}{8\eta}}(1+\cos 0)$. Once this gain is known, we turn on the FM box and aim at stabilizing $|\Psi_{\frac{\pi}{2},\frac{\pi}{2}}\rangle = (|e\rangle + i|g\rangle)/\sqrt{2}$ by setting $G_R = \sqrt{\frac{\gamma_1}{8\eta}}(1+\cos\frac{\pi}{2})$. The gain $G_{\rm FM}$ is then swept over a wide range of values. Since the simulations do not reproduce accurately the resulting data, we cannot calibrate for the unknown scaling factor accounting for the attenuation of the lines in the FM box. We heuristically use the gain $G_{\rm opt}$ for which the stabilized state has the largest coherences as a reference. To stabilize an arbitrary state $|\Psi_{\theta,\frac{\pi}{2}}\rangle$, we then choose, mimicking the controller (S25),

$$\begin{cases} G_R &= \sqrt{\frac{\gamma_1}{8\eta}}(1+\cos\theta) \\ G_{\rm FM} &= G_{\rm opt}\,\sin\theta \end{cases} . \tag{S30}$$

This supplementary degree of freedom in the choice of $G_{\rm FM}$ could lead to an increase of the coherence of the states stabilized by the experiment (red dots on Fig. 3c) compared to the predictions computed from the controller (S25) (red curve).

However the stabilized states have a reduced fidelity to the target state compared to the predictions from the simple controller (S25). In the following section, we describe Monte-Carlo simulations that were performed to take into account the experimental setup imperfections such as finite detection efficiency, electrical delays or non-linearity of the FM box, whose calibration is described in Sec. I.

B. Monte Carlo simulations

In this section, we explain how are performed the numerical simulations we use to model the experiment and investigate the effect on the feedback performance of the various parameters characterizing the setup.

Imperfections of the feedback loop such as finite propagation time lead us to perform Monte-Carlo simulations. These consist in simulating individual *quantum trajectories* [1, 2, 39] of the qubit under heterodyne detection and in presence of feedback. Each trajectory corresponds to the evolution of the qubit state on a single experiment and is conditioned on a given, simulated, output of the detector. This so called *measurement record* is randomly generated with the appropriate statistics. By averaging many such trajectories, we then reconstruct the qubit density matrix $\rho(t)$ experimentally measured by tomography.

Every trajectory simulation starts at time $t = 0$ in the state $\rho(0) = |g\rangle\langle g|$ and is run with a time step $\mathrm{d}t = 10$ ns (several times smaller than the filter characteristic times) up to a time $t \gg T_1$. At each time step $\mathrm{d}t$ we start from $\rho(t)$ and do the following.

- Generate two random numbers $\mathrm{d}W_{I,t}$ and $\mathrm{d}W_{Q,t}$ with gaussian distribution of variance $\mathrm{d}t$ that implement two independent Wiener processes.
- Compute the quadratures of the unfiltered fluorescence signal $V_{I_t}\mathrm{d}t$ and $V_{Q_t}\mathrm{d}t$ using

$$\left\{ \begin{array}{rcl} V_{I_t}\mathrm{d}t & = & \sqrt{\frac{\eta\gamma_1}{2}}\langle\sigma_x\rangle_{\rho(t)}\mathrm{d}t + \mathrm{d}W_{I,t} \\ V_{Q_t}\mathrm{d}t & = & \sqrt{\frac{\eta\gamma_1}{2}}\langle\sigma_y\rangle_{\rho(t)}\mathrm{d}t + \mathrm{d}W_{Q,t} \end{array} \right. . \tag{S31}$$

- Apply to them a $B = 3.3$ MHz first order filter modeling the JPC (Josephson Parametric Converter) finite bandwidth
  $\{V_{I_t}^{\mathrm{JPC}}, V_{Q_t}^{\mathrm{JPC}}\} = \{\ \lambda V_{I_t} + (1-\lambda)V_{I_{t-dt}}^{\mathrm{JPC}}\ ,\ \lambda V_{Q_t} + (1-\lambda)V_{Q_{t-dt}}^{\mathrm{JPC}}\ \}$, with $\lambda = \pi \mathrm{B}dt$.
- Similarly, compute the quadratures of the signal at the output of the narrow 2 MHz bandpass filter of the FM box. This filter is modeled as a fourth order filter whose parameters are determined by measuring its transfer function.
  $\{V_{I_t}^{\mathrm{FM}}, V_{Q_t}^{\mathrm{FM}}\} = \{\mathcal{F}^{(4)}(V_{I_t}^{\mathrm{JPC}}, V_{I_{t-dt}}^{\mathrm{FM}}, V_{I_{t-2dt}}^{\mathrm{FM}}, V_{I_{t-3dt}}^{\mathrm{FM}}, V_{I_{t-4dt}}^{\mathrm{FM}}), \mathcal{F}^{(4)}(V_{Q_t}^{\mathrm{JPC}}, V_{Q_{t-dt}}^{\mathrm{FM}}, V_{Q_{t-2dt}}^{\mathrm{FM}}, V_{Q_{t-3dt}}^{\mathrm{FM}}, V_{Q_{t-4dt}}^{\mathrm{FM}})\}$.
  Note that since the other filters have bandwidths much larger than the one of the JPC, their effect on the signal shape is negligible. The corresponding group delays simply contribute to the total propagation time across the lines (see Sec. I D).
- Compute the values of the control parameters $\delta u_t, \delta v_t$ and w_t.

$$\begin{pmatrix} \delta u_t \\ \delta v_t \end{pmatrix} = G_R \times \begin{pmatrix} \cos\alpha & \sin\alpha \\ -\sin\alpha & \cos\alpha \end{pmatrix} \times \begin{pmatrix} V_{I_t}^{\mathrm{JPC}} \\ V_{Q_t}^{\mathrm{JPC}} \end{pmatrix}, \tag{S32}$$

$$w_t = G_{\mathrm{FM}} \times (\cos\beta\ \ \sin\beta)\ .\ \begin{pmatrix} V_{I_t}^{\mathrm{FM}} \\ V_{Q_t}^{\mathrm{FM}} \end{pmatrix} + e \times G_{\mathrm{FM}}^2 \times \left((V_{I_t}^{\mathrm{FM}})^2 + (V_{Q_t}^{\mathrm{FM}})^2\right). \tag{S33}$$

  The parameter e models the small non-linearity of the Stark shift $\delta f(t)$ of the qubit frequency. It is measured by fitting with a quadratic law the dependency of δf on V_β and $V_{\beta+\frac{\pi}{2}}$ (continuous lines in Fig. S5).
- Compute the control hamiltonian by taking into account the finite propagation times of the signal
  $H_t^{\mathrm{cont}} = (\overline{u} + \delta u_{t-T_{\mathrm{Rabi}}})\sigma_x + (\overline{v} + \delta v_{t-T_{\mathrm{Rabi}}})\sigma_y + w_{t-T_{\mathrm{FM}}}\sigma_z$.
- Compute the open loop evolution using

$$\rho_{\mathrm{open}}(t+\mathrm{d}t) = \frac{M_t\rho(t)M_t^\dagger + (1-\eta)\gamma_1\sigma_-\rho(t)\sigma_+\mathrm{d}t + \gamma_\phi/2\sigma_z\rho(t)\sigma_z\mathrm{d}t}{\mathrm{Tr}[M_t\rho(t)M_t^\dagger + (1-\eta)\gamma_1\sigma_-\rho(t)\sigma_+\mathrm{d}t + \gamma_\phi/2\sigma_z\rho(t)\sigma_z\mathrm{d}t]}, \tag{S34}$$

  where the Kraus operator M_t depends on the measurement records at time t as

$$M_t = \mathbf{1} - (iH_0 + iH_{\mathrm{drift}} + \frac{\gamma_1}{2}\sigma_+\sigma_- + \frac{\gamma_\phi}{4}\mathbf{1})\mathrm{d}t + \sqrt{\frac{\eta\gamma_1}{2}}(\sigma_- V_{I_t}\mathrm{d}t + i\sigma_- V_{Q_t}\mathrm{d}t). \tag{S35}$$

  We use here a numerically more stable formulation than Eq. (S19) for the SME in open loop [40].
- Compute the density matrix $\rho(t+\mathrm{d}t)$ after action of the feedback as $\rho(t+dt) = e^{-iH_t^{\mathrm{cont}}dt}\rho_{\mathrm{open}}(t+dt)e^{+iH_t^{\mathrm{cont}}dt}$.

C. Role of each parameter on the state purity

All the parameters entering in the simulations whose results are in the Letter ($\gamma_1, \gamma_\phi, \eta, T_{\mathrm{Rabi}}, T_{\mathrm{FM}}, e, B$ and the characteristic times of the 2 MHz bandpass) were measured independently, as explained in the previous sections of the Supplementary Material. In order to get a better sense of how to explain the discrepancy between the measured states and the expected ones, we here investigate numerically the effect of each of them on the stabilized states.

Modified parameter	max stable excitation	max stable $\langle\sigma_y\rangle$
none (as measured)	59 %	56 %
$\beta = 0$ instead of $-10°$	59 %	56 %
$\eta = 1$ instead of 0.35	**95 %**	**66 %**
$T_\phi = \infty$ instead of 22 μs	59 %	**69 %**
$e = 0$ instead of 64 ns (FM non-linearity)	59 %	57 %
no 2 MHz bandpass (but the JPC is still there)	59 %	**53 %**
no propagation delay instead of 120 ns	60 %	56 %
without JPC and 2 MHz filter and with $e = 0$	59 %	55 %

Table I: Summary of the impact of each parameter on the maximal coherence (more precisely $\langle\sigma_y\rangle$) and excitation probability that can be stabilized according to Monte Carlo simulations. Note that experimentally, we find 59 % of excitation $((1+\langle\sigma_z\rangle)/2$ and 43 % for $\langle\sigma_y\rangle$ at max.

In Table I are summarized the predicted deviations to the maximal values of excitation and $\langle\sigma_y\rangle$ that one can stabilize according to simulations using various alterations on the independently measured parameters. The full results of these simulations is shown in Fig. S8 together with the experimental results.

From these figures, we arrive at the following conclusions:

- The performance of our feedback scheme is mainly limited by the finite detection efficiency $\eta = 0.35$. It appears that it is the only parameter that can visibly affect the maximal excitation probability of the stabilized state. The good match between the experimental value of maximal excitation and the predicted one implies that η is compatible with our measurement.
- Qubit dephasing clearly limits the coherence of stabilized states. Having underestimated it (for a reason we could not determine) could explain the discrepancy between experiment and simulations.
- The 2 MHz bandpass filter slightly improves the performance of the feedback. This observation is consistent with a narrow filtering of the white thermal noise coming from the finite detection inefficiency. Note that in the experiment, this classical noise is even larger before filtering due to imperfect components (noisy room temperature amplifiers, imperfect rejection of the unwanted side-band of the mixers...), which motivated us to add this filter in the first place.
- In the experiment, a non-zero $\langle\sigma_x\rangle$ appears when $\theta \neq 0, \pi$. Such a deviation to 0 is also obtained with a small non-linearity of the Stark shift (compare blue points) or when considering a finite detuning of the drift terms compared to the qubit frequency (not shown). Note that for the simulations appearing in the Letter (reproduced in red points here), we set a small angle $\beta = -10°$ in order to have $\langle\sigma_x\rangle = 0$ when $\theta = \pi/2$, as was done experimentally. The sign of $\langle\sigma_x\rangle$ is not reproduced in the simulations unless an additional detuning of the drift terms is considered. Nonetheless, we see here that neither the small shift of β, nor the small Stark non-linearity e, have a visible impact on the stabilized value of $\langle\sigma_y\rangle$ and $\langle\sigma_z\rangle$.
- The time delays, which are much shorter than T_1, do not appear to have a significant impact.

D. Discussion about a possible underestimation of the dephasing rate

As shown in Table I, the discrepancy between experiment and simulation on the value of the coherence of stabilized states could originate from an underestimation of the dephasing rate during feedback. As explained in section I A, the dephasing rate has two contributions: a constant term $\gamma^* = (30\ \mu\mathrm{s})^{-1}$ corresponding to pure dephasing, which is present in absence of any drive, and measurement induced dephasing, which depends on the signals we sent near the cavity frequency.

In this section, we investigate what is the exact dephasing rate in presence of feedback. Indeed, the FM box uses ac-Stark effect to detune the qubit by a controlled amount $w(t)$, which means that a residual measurement induced dephasing γ_m is also present. We have tested two levels of approximations about γ_m.

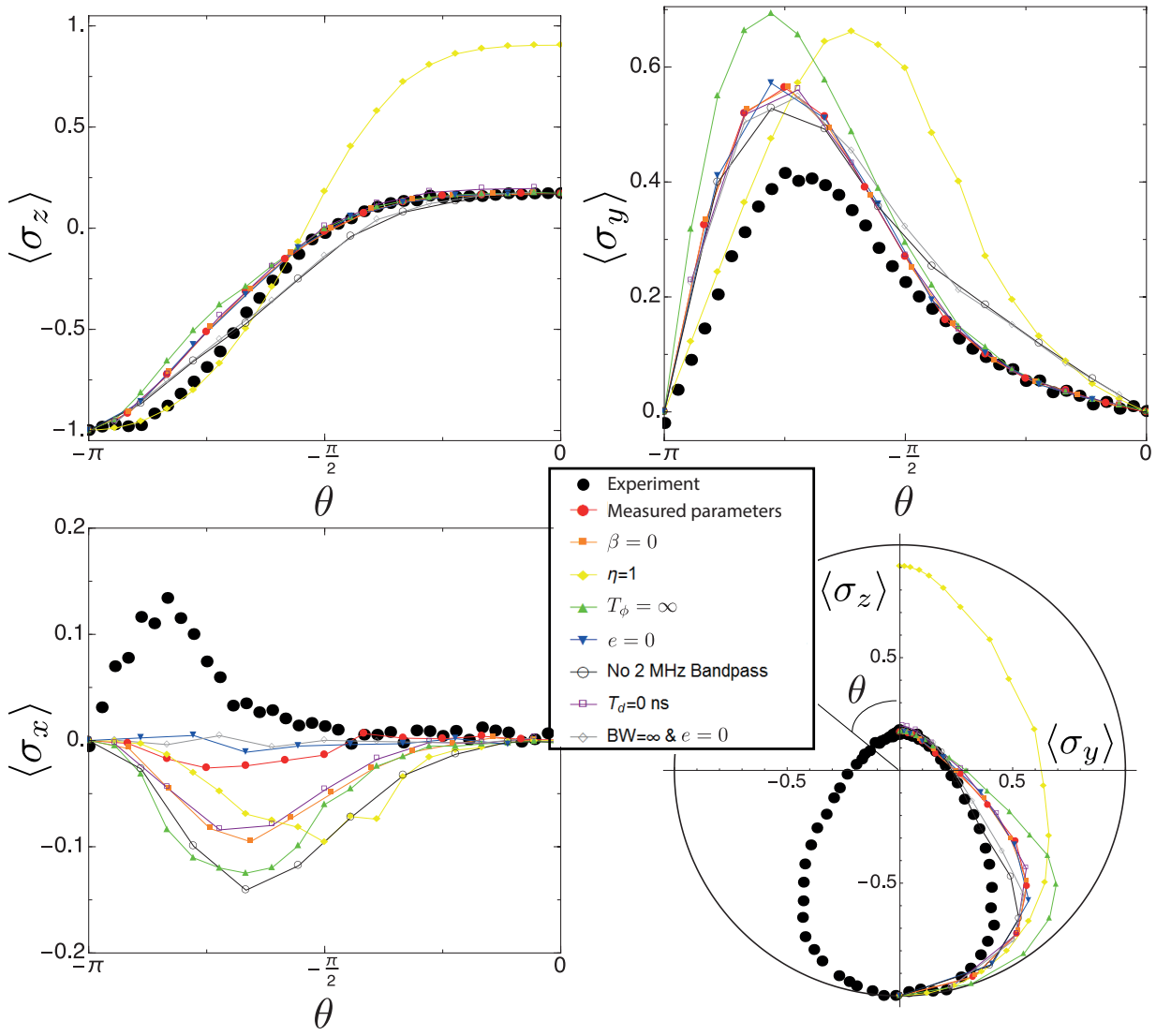

Figure S8: Results of the simulation for various alterations of its parameters. Each panel represents a different projection of the Bloch vectors of the states that are predicted to be stabilized for all values of θ. The experimentally stabilized states are shown as black dots for reference. The simulation results corresponding to the values of parameters that were independently measured are shown in red. Every other curve represents the results of the same simulation when at least one parameter is modified (see Table I)

- First, we have assumed that γ_m is constant despite the fluctuations of $w(t)$ associated with the feedback protocol. Using Ramsey interferometry when the drive with large amplitude ϵ_0 is turned on in the FM box (but $w = 0$), we find $\gamma_m = (84\ \mu\text{s})^{-1}$. This is the value we have used in all this work.

- Second, we can simulate the full dynamics of the cavity+qubit system in presence of feedback. It would be possible that the variations of γ_m in time due to the inputs of the MIMO controller lead to a decrease of the coherence of stabilized states. With that aim, we compute the evolution of the fields α_g and α_e for a small enough time step $\mathrm{d}t = 0.5$ ns as

  $$\alpha_{g,e}(t+\mathrm{d}t) = \alpha_{g,e}(t) + \alpha_{g,e}(t)\left(2i\pi(\Delta \mp \tfrac{\chi}{2}) - \tfrac{\kappa}{2}\right)\mathrm{d}t + G' e^{i\beta}\left(\epsilon_0 + G(V_\beta^{\mathrm{FM}} + iV_{\beta+\pi/2}^{\mathrm{FM}})\right)\mathrm{d}t,$$

  where G, G' and $\epsilon_0 e^{i\beta}$ are those appearing in Eq. (S9). These parameters of the simulations are determined by matching the detuning of Eq. (S9) to the measured one Eq. (S33). Then, we compute the Stark shift and the pure dephasing induced on the qubit state by the measurement performed by this tone probing the cavity as

  $$\begin{aligned} w(t) &= 2\pi\chi\mathrm{Re}[\alpha_e(t)\alpha_g(t)^*] \\ \gamma_m(t) &= 2\pi\chi\mathrm{Im}[\alpha_e\alpha_g^*] \end{aligned}.$$

We have performed simulations with both assumptions and show the resulting expected stabilized states in Fig. S9. It appears that both assumptions have identical effects on the predicted coherence. This validates the approach of the first assumption that we have used throughout the present work.

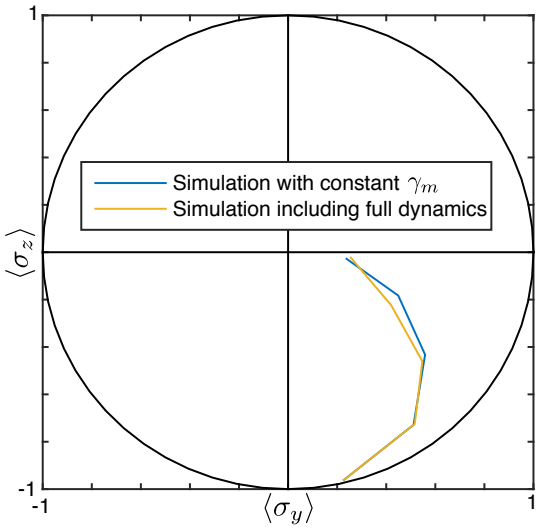

Figure S9: Results of simulations with both approximations about measurement induced dephasing. Note that for the simulation including the cavity dynamics we have neglected the small effect of the out-of-phase signal by putting $V^{\mathrm{FM}}_{\beta+\pi/2} \simeq 0$.

[1] H. Carmichael, "Quantum trajectory theory for cascaded open systems," *Physical review letters*, vol. 70, no. 15, p. 2273, 1993.

[2] H. M. Wiseman and G. J. Milburn, *Quantum measurement and control*. Cambridge University Press, 2009.

[3] P. Campagne-Ibarcq, P. Six, L. Bretheau, A. Sarlette, M. Mirrahimi, P. Rouchon, and B. Huard, "Observing Quantum State Diffusion by Heterodyne Detection of Fluorescence," *Phys. Rev. X*, vol. 6, p. 11002, jan 2016.

[4] M. Naghiloo, N. Foroozani, D. Tan, A. Jadbabaie, and K. Murch, "Mapping quantum state dynamics in spontaneous emission," *Nature communications*, vol. 7, 2016.

[5] H. Hofmann, G. Mahler, and O. Hess, "Quantum control of atomic systems by homodyne detection and feedback," *Physical Review A*, vol. 57, no. 6, pp. 4877–4888, 1998.

[6] J. Wang and H. M. Wiseman, "Feedback-stabilization of an arbitrary pure state of a two-level atom," *Physical Review A*, vol. 64, no. 6, p. 063810, 2001.

[14] A. Chia and H. M. Wiseman, "Quantum theory of multiple-inputâĂŞmultiple-output Markovian feedback with diffusive measurements," *Physical Review A*, vol. 84, no. 1, p. 012120, 2011.

[17] E. M. Purcell, "Proceedings of the American Physical society, Spontaneous Emission Probabilities at Radio Frequencies," *Phys. Rev.*, vol. 96, 681, 1946.

[18] N. Bergeal, F. Schackert, M. Metcalfe, R. Vijay, V. E. Manucharyan, L. Frunzio, D. E. Prober, R. J. Schoelkopf, S. M. Girvin, and M. H. Devoret, "Phase-preserving amplification near the quantum limit with a Josephson ring modulator," *Nature*, vol. 465, pp. 64–68, may 2010.

[19] N. Roch, E. Flurin, F. Nguyen, P. Morfin, P. Campagne-Ibarcq, M. H. Devoret, and B. Huard, "Widely Tunable, Nondegenerate Three-Wave Mixing Microwave Device Operating near the Quantum Limit," *Physical Review Letters*, vol. 108, p. 147701, apr 2012.

[22] A. A. Houck, D. I. Schuster, J. M. Gambetta, J. A. Schreier, B. R. Johnson, J. M. Chow, L. Frunzio, J. Majer, M. H. Devoret, S. M. Girvin, and R. J. Schoelkopf, "Generating single microwave photons in a circuit," *Nature*, vol. 449, pp. 328–331, jan 2007.

[24] H. Wiseman, "Quantum theory of continuous feedback," *Physical Review A*, vol. 49, no. 3, p. 2133, 1994.

[25] J. Gambetta, A. Blais, D. Schuster, A. Wallraff, L. Frunzio, J. Majer, M. Devoret, S. Girvin, and R. Schoelkopf, "Qubit-photon interactions in a cavity: Measurement-induced dephasing and number splitting," *Physical Review A*, vol. 74, p. 042318, Oct. 2006.

[26] A. Blais, J. Gambetta, A. Wallraff, D. I. Schuster, S. M. Girvin, M. H. Devoret, and R. J. Schoelkopf, "Quantum-information processing with circuit quantum electrodynamics," *Physical Review A*, vol. 75, no. 3, p. 032329, 2007.

[31] H. Paik, D. I. Schuster, L. S. Bishop, G. Kirchmair, G. Catelani, a. P. Sears, B. R. Johnson, M. J. Reagor, L. Frunzio, L. I. Glazman, S. M. Girvin, M. H. Devoret, and R. J. Schoelkopf, "Observation of High Coherence in Josephson Junction Qubits Measured in a Three-Dimensional Circuit QED Architecture," *Physical Review Letters*, vol. 107, p. 240501, dec 2011.

[32] S. E. Nigg, H. Paik, B. Vlastakis, G. Kirchmair, S. Shankar, L. Frunzio, M. Devoret, R. Schoelkopf, and S. Girvin, "Black-box superconducting circuit quantization," *Direct*, 2012.

[32] K. L. Geerlings, *Improving Coherence of Superconducting Qubits and Resonators*. PhD thesis, YALE UNIVERSITY, 2013.

[34] O. Astafiev, A. Abdumalikov Jr, A. M. Zagoskin, Y. A. Pashkin, Y. Nakamura, and J. Tsai, "Ultimate on-chip quantum amplifier," *Physical review letters*, vol. 104, no. 18, p. 183603, 2010.

[35] A. Abdumalikov Jr, O. Astafiev, Y. A. Pashkin, Y. Nakamura, and J. Tsai, "Dynamics of coherent and incoherent emission from an artificial atom in a 1D space," *Physical review letters*, vol. 107, no. 4, p. 043604, 2011.

[36] P. Campagne-Ibarcq, L. Bretheau, E. Flurin, A. Auffèves, F. Mallet, and B. Huard, "Observing interferences between past and future quantum states in resonance fluorescence," *Physical review letters*, vol. 112, no. 18, p. 180402, 2014.

[37] J. Gambetta, A. Blais, M. Boissonneault, A. Houck, D. Schuster, and S. Girvin, "Quantum trajectory approach to circuit QED: Quantum jumps and the Zeno effect," *Physical Review A*, vol. 77, no. 1, p. 012112, 2008.

[38] H. M. Wiseman, S. Mancini, and J. Wang, "Bayesian feedback versus markovian feedback in a two-level atom," *Physical Review A*, vol. 66, no. 1, p. 013807, 2002.

[39] A. Barchielli and M. Gregoratti, *Quantum Trajectories and Measurements in Continuous Time*, vol. 782. Springer-Verlag Berlin Heidelberg, 2009.

[40] P. Rouchon, and J.F. Ralph, "Efficient quantum filtering for quantum feedback control," *Physical Review A*, vol. 91, p. 012118, 2015.